Article

Not peer-reviewed version

Observations of Crab Pulsar Giant Pulses with the Parkes Ultra-Wideband (UWL) Receiver

Langin Wang , Rushuang Zhao * , Hui Liu , Zefeng Tu , Ruwen Tian , Hongwei Xu , Quan Zhou , Dongyang Yan , Yi Zhou , Kun Yang , Junjie Feng

Posted Date: 15 April 2026

doi: 10.20944/preprints202604.1002.v1

Keywords: Crab pulsar; giant pulses; ultra-wideband observations; spectral properties; temporal structure; energy statistics

 doi:10.20944/preprints202604.1002.v1

Article

Observations of Crab Pulsar Giant Pulses with the Parkes Ultra-Wideband (UWL) Receiver

Lanqin Wang [1], Rushuang Zhao [1,*], Hui Liu [1], Zefeng Tu [1], Ruwen Tian [2], Hongwei Xu [3], Quan Zhou [1], Dongyang Yan [1], Yi Zhou [1], Kun Yang [4] and Junjie Feng [5]

[1] School of Physics and Electronic Science, Guizhou Normal University, Guiyang 550025, China
[2] Guangxi University, Nanning 530004, China
[3] Central China Normal University, Wuhan 430079, China
[4] Minzu Normal University of Xingyi, Xingyi 562400, China
[5] Liupanshui Normal University, Liupanshui 553004, China
* Correspondence: 201907007@gznu.edu.cn

Abstract

We present a systematic study of giant pulses (GPs) from the Crab pulsar (PSR J0534+2200) using ultra-wideband observations with the Parkes radio telescope. We introduce an empirical classification scheme based on the cumulative distribution function (CDF) of pulse energy in frequency, separating the detected events into narrow-band and broadband GPs, with the former dominating the present sample. The narrow-band events concentrate most of their energy within limited frequency ranges, whereas broadband events show more extended spectral coverage. Spectral fitting shows that most narrow-band GPs have negative spectral indices, while a few events exhibit positive slopes, indicating substantial spectral diversity within the sample. The 3σ widths of narrow-band main pulse GPs appear to cluster around two characteristic ranges, although this feature should be interpreted with caution given the time resolution of the data. The energy distribution of narrow-band main pulse GPs is broadly consistent with a log-normal form at low-to-intermediate energies and a power-law-like tail at the high-energy end. The waiting-time distribution can be described by a Weibull function, while a sliding-window comparison with Monte Carlo Poisson realizations shows no statistically significant deviation from temporal independence over the present 18.9-minute observing span. These results provide observational constraints on the phenomenology of Crab giant pulses and may be useful for future studies of pulsar coherent emission and related radio transients.

Keywords: Crab pulsar; giant pulses; ultra-wideband observations; spectral properties; temporal structure; energy statistics

1. Introduction

The Crab pulsar (PSR J0534+2200) is one of the most prominent young pulsars in the Milky Way. Its extremely high spin-down power and strong magnetic field environment make it an ideal natural laboratory for studying particle acceleration and coherent radiation processes under extreme conditions [1,2]. The pulsar emits GPs, which are extremely short-duration bursts with instantaneous flux densities exceeding the average pulse by several orders of magnitude. Since their first discovery, GPs have been considered an important observational window for probing nonlinear plasma processes and coherent emission mechanisms in pulsar magnetospheres [3,4].

Over the past few decades, studies of Crab pulsar GPs have mainly focused on their extreme temporal structures, energy distributions, and associations with the main pulse and interpulse phases. Very Long Baseline Interferometry (VLBI) observations have confirmed that GPs emission originates within the pulsar magnetosphere rather than in the nebular shock regions [5]. Numerous observations indicate that the energy distribution of GPs often follows a power-law at the high-energy end, suggesting a generation process characterized by scale-free nonlinear amplification or critical behavior [6–8].

 doi:10.20944/preprints202604.1002.v1

In the time domain, microsecond- and even nanosecond-scale fine structures have been repeatedly reported, implying extremely small emission regions and highly coherent radiation processes [9,10].

However, due to the limited bandwidth of early receivers, most studies were confined to relatively narrow frequency ranges (typically tens to hundreds of MHz), making it difficult to systematically characterize the spectral behavior of GPs over wide frequency ranges and their frequency-dependent emission properties. Existing observations indicate that GPs can exhibit significantly different spectral shapes and bandwidths at different frequencies, suggesting that their emission mechanisms or regions are not singular [8,11]. In recent broadband observations, a class of narrow-band GPs has been identified, with spectral widths significantly smaller than those of conventional broadband GPs when expressed as a fraction of the central frequency ($\Delta\nu/\nu$). Using observations from the 46-m telescope in the 400–800 MHz range, Thulasiram & Lin (2021) identified a subpopulation of narrow-band GPs with $\Delta\nu/\nu \simeq 0.1$, appearing in both main pulse and interpulse phases. This finding supports an intrinsic emission mechanism rather than propagation effects [12]. Nevertheless, current distinctions between "narrow-band" and "broadband" GPs largely rely on empirical frequency coverage or subjective thresholds, lacking a unified and reproducible quantitative classification standard.

With the commissioning of the Parkes Ultra-Wideband Low receiver (UWL) [13], continuous coverage of 732–4032 MHz in a single observation has become possible. This provides an unprecedented opportunity to systematically study the time-frequency characteristics, spectral morphology, and statistical properties of Crab pulsar GPs under broadband conditions. At the same time, the increased data volume poses higher demands for objective GPs identification, bandwidth quantification, and statistical comparison of different emission properties.

PSR J0534+2200 is one of the most active known GP emitters [3,6,8], and its narrow-band and broadband emission properties under ultra-wideband conditions remain important observational issues. In this work, we present a systematic analysis of Crab pulsar GPs using Parkes UWL observations. Specifically, we: (1) introduce a reproducible empirical framework based on the cumulative distribution function (CDF) of pulse energy to characterize the frequency-domain extent of individual GPs; (2) compare narrow-band and broadband events in terms of spectral indices, temporal widths, and energy distributions within this framework; and (3) investigate their temporal behavior through waiting-time statistics and sliding-window burst-rate analysis [6,14]. Our aim is to provide observational constraints on the diversity of Crab GPs under wideband conditions, while also clarifying the statistical limitations of the current dataset.

2. Observations and Data Analysis

2.1. Observational Setup and Data Acquisition

The observational data used in this study were obtained from the PX500 project of the National Astronomical Observatories, Chinese Academy of Sciences. On 27 June 2024, targeted observations of the Crab pulsar (PSR J0534+2200) were carried out with the 64-m Parkes radio telescope in Australia. The observations employed the Ultra-Wideband Low (UWL) receiver [13], providing continuous frequency coverage from 732 to 4032 MHz, with a central frequency of 2382 MHz and an effective integration time of 18.9 minutes. Raw voltage data were recorded in real time by the Parkes digital backend. It should be noted that no absolute flux calibration was performed during the observations; thus, all intensity and energy analyses in this work are based on relative units, which are sufficient for comparing different GPs events and discussing emission mechanisms [11].During the data acquisition stage, coherent dedispersion was applied to remove the dispersive delays caused by the interstellar medium, using a dispersion measure of DM = 56.72 pc cm^{-3} [6,9]. The time resolution of the processed data is 128 μs, which is adequate to resolve the emission structure within a single pulsar rotation. Subsequently, single-pulse folding was performed using the `DSPSR` software package [16], based on the precise ephemeris of PSR J0534+2200 (spin period $P = 33.502$ ms), with each rotation divided into 256 uniform phase bins. The resulting phase-aligned single-pulse profile sequence preserves the

 doi:10.20944/preprints202604.1002.v1

phase information of both the main pulse (MP) and interpulse (IP), providing a solid foundation for subsequent single-pulse statistics and broadband emission analysis.

2.2. Radio Frequency Interference Excision

Broadband radio observations are inevitably affected by various forms of radio frequency interference (RFI). To ensure reliable GPs identification and statistical analysis, a systematic RFI excision procedure was applied during data processing. RFI mitigation was primarily conducted using the `PSRCHIVE` software package [17,18]. In the frequency domain, persistently contaminated narrow-band channels were identified based on their statistical properties and subsequently masked. In the time domain, anomalous time samples deviating from the noise distribution were removed to eliminate transient strong interference events [19]. All thresholds applied in the RFI excision process were determined according to the statistical characteristics of the data itself, minimizing potential systematic biases on the genuine astrophysical signals. In addition, a subset of the automatically processed data was visually inspected, examining dynamic spectra and pulse profiles to further remove any remaining abnormal interference events. After these procedures, the data quality was deemed sufficient for subsequent GPs selection and broadband statistical analyses.

2.3. Giant Pulses Selection Criteria and Data Set Construction

To reliably extract GPs events from the large single-pulse dataset, a dual selection criterion based on relative intensity and signal-to-noise ratio (SNR) was employed. First, an initial selection was made based on pulse intensity. The peak of each candidate GPs profile was required to exceed 30 times the mean peak of all single-pulse profiles. This threshold ensures that selected events are significantly distinct from regular pulses in terms of emission strength, allowing clear separation from ordinary pulsar emission. Subsequently, to further exclude random noise fluctuations and low-SNR events, all candidate pulses were required to satisfy SNR > 9. This dual criterion preserves the purity of the GPs sample while avoiding overly conservative selection bias.

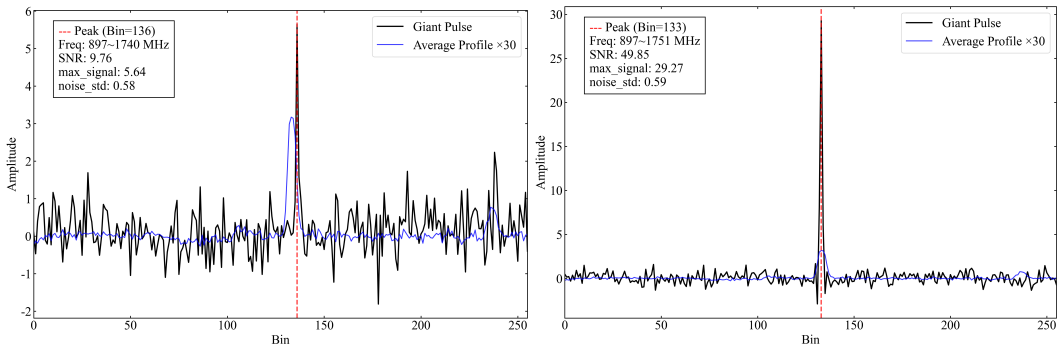

(**a**) (**b**)

Figure 1. This figure shows two GPs events selected through the dual selection procedure in this observation. The black solid line represents the intensity variation of each GPs across 256 phase bins, while the blue dashed line shows 30 times the mean profile of all pulses, illustrating the significant enhancement of the GPs relative to the average emission. (a) The event has a signal-to-noise ratio (SNR) of 9.76, satisfying both criteria of SNR > 9 and a peak exceeding 30 times the mean profile peak, representing one of the weakest GPs that still exhibits a clearly discernible profile. (b) The event is a high-SNR GPs, with SNR well above 9.

Figure 1 presents two typical GPs examples identified through the above selection procedure.(a) shows an event with a signal-to-noise ratio (SNR) of 9.76, which is one of the weakest GPs that satisfy the selection criteria, yet its pulse profile remains clearly discernible.(b) displays a high-SNR, strong GPs event. Both exhibit peak features that are significantly enhanced relative to the average profile. For all candidate events selected based on both intensity and SNR, their peak phases were further checked to determine whether they fall within the known main pulse or interpulse phase windows.

 doi:10.20944/preprints202604.1002.v1

This phase consistency check effectively prevents residual radio frequency interference (RFI) events from being misclassified as genuine GPs, thereby improving the physical reliability of the sample. Using this procedure, a total of 372 high-confidence GPs were identified out of 33,531 pulse periods.

3. Results and Analysis

3.1. Narrow-Band Giant Pulses

3.1.1. Energy Cumulative Distribution Function (CDF) Method

To quantitatively characterize the energy distribution of GPs in the frequency domain and to distinguish between narrow-band and broadband GPs, we applied the cumulative distribution function (CDF) method to each individual GPs event. For each pulse, the on-pulse and off-pulse regions were selected from the two-dimensional time-frequency dynamic spectrum as the signal and background references, respectively. The on-pulse region is defined as the portion of the dynamic spectrum where the signal intensity exceeds the background noise by more than 3σ, concentrating the main emission and energy of the GP. The off-pulse region, with the same width as the on-pulse window, contains no significant pulse emission and serves as a reference for background noise. By computing the cumulative distribution of signal energy across frequencies within the on-pulse region and subtracting the corresponding off-pulse cumulative energy, we obtain the net energy CDF curve. This curve describes the cumulative contribution of pulse energy as a function of frequency, directly reflecting whether the energy is concentrated or dispersed in the frequency domain. Subsequently, the net energy CDF curve is fitted using a piecewise linear approach. Candidate cutoff frequencies are uniformly selected from the middle portion of the cumulative energy range, excluding the lowest and highest 5% of data points to avoid edge effects. For each candidate cutoff frequency, the optimal piecewise linear fit is determined via the least-squares method, and the cutoff corresponding to the minimum residual sum of squares (RSS) is chosen as the best estimate. This cutoff frequency indicates the point where the cumulative energy behavior changes significantly and is used to characterize the effective frequency range of the pulse.To assess the statistical uncertainty of the cutoff frequency, an error band is constructed based on the mean and standard deviation of each fitting interval. The upper and lower boundaries of the error band are separately fitted, and the resulting intersection range provides an estimate of the cutoff frequency uncertainty. This method avoids subjective threshold selection while providing a quantifiable measure of uncertainty for subsequent statistical analyses.

3.1.2. Classification of Narrow-Band and Broadband Giant Pulses

Based on the CDF analysis described above, each detected GP was examined individually in the frequency domain. In this work, we adopt an empirical but reproducible classification scheme. Events whose net cumulative energy rises rapidly over a limited frequency interval and then approaches a plateau are classified as narrow-band GPs. In contrast, events whose net cumulative energy continues to increase over a much broader frequency range, without an early flattening trend, are classified as broadband GPs. The cutoff frequency derived from the piecewise fit is used as a convenient descriptor of the effective upper extent of the dominant emission.

Figure 2 presents representative examples of the two classes. In Figure 2(a), the emission is primarily concentrated within a restricted frequency range, and the net CDF becomes nearly flat above the main emitting band. In Figure 2(b), the emission extends over a substantially wider frequency interval, and the corresponding net CDF continues to increase to higher frequencies. Applying this empirical scheme to the full sample, we identify 353 narrow-band and 19 broadband GPs (Table 1). We stress that this classification is intended as a practical description of the present dataset rather than a unique physical taxonomy, and its robustness should be further examined with larger samples and alternative model-selection criteria. To provide a more detailed overview of the individual giant pulses, the measured parameters of all detected events, including normalized pulse energy, signal-to-noise ratio, central frequency, bandwidth, relative bandwidth, and spectral index, are listed in Appendix A1(Table A1).

 doi:10.20944/preprints202604.1002.v1

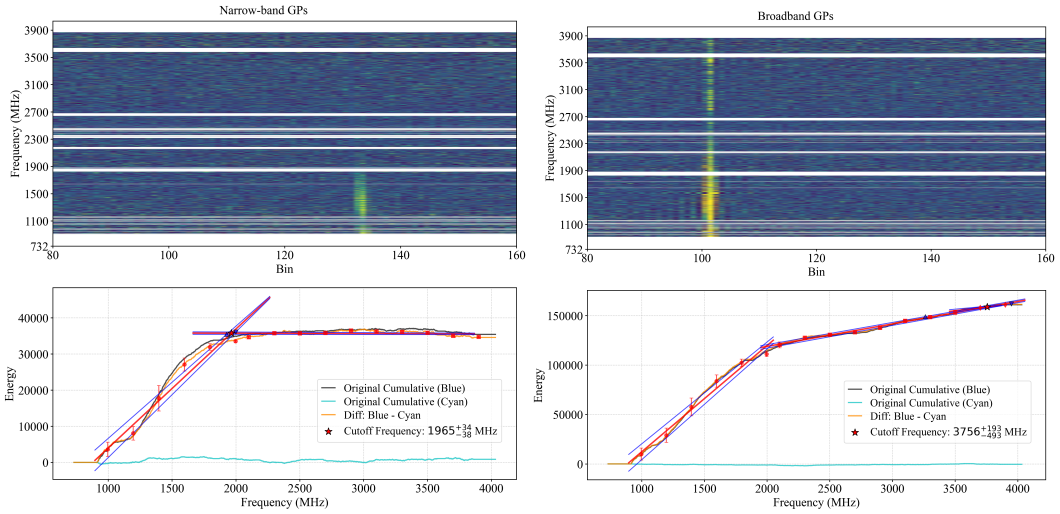

Figure 2. Typical features of a narrow-band and a broadband GPs from the Crab pulsar, shown in panels (a) and (b), respectively. The upper sub-panels display the spectra, while the lower sub-panels show the cumulative energy distribution (CDF) curves. In the CDF plots, the black curve represents the cumulative energy in the on-pulse region, the light blue curve represents the cumulative energy in the off-pulse region, and the orange curve represents the net energy obtained by subtracting the off-pulse CDF from the on-pulse CDF. The red curve shows the piecewise linear fit to the data, and the dark blue curve indicates the fitting uncertainty. The red star marks the "cutoff frequency" of the pulse energy, while the blue triangle denotes the associated uncertainty range.

Figure 2 highlights the contrast between the two spectral morphologies considered in this work. The narrow-band example shows that most of the pulse energy is confined to a limited spectral interval, whereas the broadband example exhibits enhanced emission over a much larger frequency span. The corresponding CDF curves provide a compact way to visualize how rapidly the pulse energy accumulates with frequency and where it begins to saturate. In this sense, the CDF-based representation is useful for comparing events with different spectral extents in a uniform manner.

3.1.3. Phase Distribution of Narrow-Band and Broadband Giant Pulses

After determining the bandwidth class of each GP, we further assigned each event to either the main pulse (MP) or interpulse (IP) phase window according to the phase of its peak. Among the 353 narrow-band GPs, 335 occur in the MP window and 18 in the IP window. Among the 19 broadband GPs, 17 are found in the MP window and 2 in the IP window (Table 1). Thus, both classes are dominated by MP events in the present dataset. Because the IP and broadband subsamples are both small, the apparent differences between phase categories should be interpreted with caution. A statistical comparison based on the current counts does not provide strong evidence for a significant association between pulse phase and bandwidth class. We therefore regard the present result mainly as a descriptive summary of the observed sample rather than a firm population-level conclusion.

Table 1. Numbers of narrow-band and broadband giant pulses detected in the main pulse (MP) and interpulse (IP) phase windows.

	Narrow-band	**Broadband**	**Total**
MP	335	17	352
IP	18	2	20
Total	353	19	372

 doi:10.20944/preprints202604.1002.v1

3.1.4. Statistical Properties of Relative Bandwidth for Narrow-Band Giant Pulses

Based on the classification described above, we further performed a statistical analysis of the relative bandwidth of narrow-band GPs. The dimensionless parameter defined as the ratio of the frequency bandwidth to the central frequency was used to characterize the relative concentration of emission in the frequency domain. Figures 3(a) and 3(b) show the histograms of the relative bandwidth distribution for narrow-band GPs in the main pulse and interpulse, respectively. For the main pulse sample, the relative bandwidth distribution exhibits a clear bimodal structure. A double-Gaussian model provides a good fit to describe this feature, with one peak centered around 0.65 with a relatively narrow width, and another peak around 0.74 with a broader spread. For the MP-narrow-band sample, the histogram shows a possible bimodal tendency, and a double-Gaussian function provides a visually reasonable description of the distribution. However, the statistical significance of this apparent bimodality should be tested more rigorously in future work using model-comparison criteria such as AIC, BIC, or bootstrap resampling. For the IP-narrow-band sample, only 18 events are available, and no robust statement about the underlying distribution can be made from the present data.

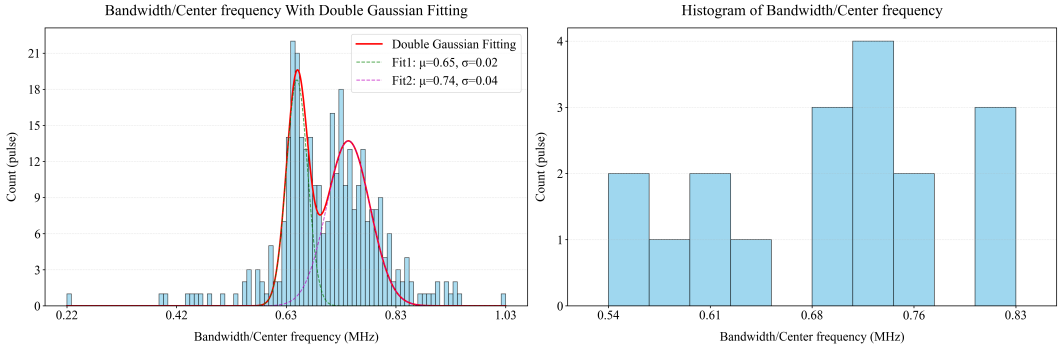

(**a**) (**b**)

Figure 3. Histograms of the relative bandwidth (ratio of narrow-band bandwidth to central frequency) for narrow-band GPs in the main pulse and interpulse , shown in panels (a) and (b), respectively. In panel (a), the red curve represents the double-Gaussian fit to the main pulse distribution. The green and purple curves represent single-Gaussian fits to the same main pulse distribution.

3.2. Spectral Index Properties of Giant Pulses

To further characterize the spectral behavior of narrow-band and broadband GPs, we performed a power-law fit to the energy spectrum of each individual GPs. The fit adopts the following form:

$$F_\nu = C\,\nu^{\alpha}, \tag{1}$$

where F_ν is the peak flux at frequency ν, C is a normalization constant, and α is the spectral index used to describe the overall steepness of the spectrum.

3.2.1. Spectral Morphology of Representative Pulses

Despite the dominance of narrow-band GPs within the main pulse phase window (approximately 94.9%), their spectral behavior is not uniform and exhibits significant heterogeneity. Figure 4 shows the spectra of two representative narrow-band GPs, which display opposite trends in their frequency–flux relationships: one exhibits a typical power-law decay, while the other shows a power-law increase. Figure 4(a) presents a narrow-band GPs with a negative spectral slope. Its spectrum, spanning approximately 750–1900 MHz, clearly follows a power-law decay, with a fitted spectral index of $\alpha \approx -3.17 \pm 0.30$, indicating a stable spectral structure with strong power-law characteristics and a significant decrease in flux with increasing frequency. In contrast, Figure 4(b) illustrates a narrow-band GPs with a positive spectral slope. In the low-frequency region, the flux increases monotonically with

 doi:10.20944/preprints202604.1002.v1

frequency, yielding a fitted spectral index of $\alpha \approx 1.45 \pm 0.22$. This "high-frequency enhanced" spectral feature is extremely rare among narrow-band GPs [20].

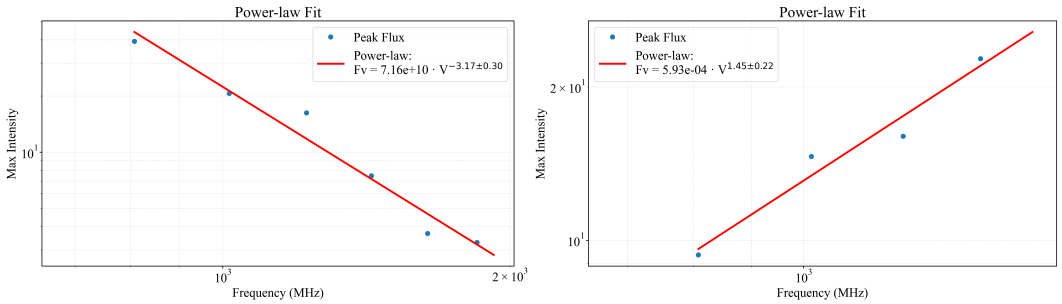

(**a**) (**b**)

Figure 4. Spectral morphology of two representative narrow-band GPs, shown in panels (a) and (b), respectively. Blue circles indicate the peak flux at different frequency bands, while the red curves represent the power-law fits to the data. The spectral index α characterizes the slope of each fit.

3.2.2. Statistical Distribution of Spectral Indices

A statistical analysis of the spectral indices for the full sample further quantifies the systematic differences in spectral characteristics between different types of giant GPs. Figure 5(a) shows the histogram of spectral indices for the main pulse and the corresponding single-Gaussian fit. The spectral indices of the MP-narrow-band sample span a wide range from -4.56 to 1.45, including both negative and positive values. This result is consistent with the observations of Karuppusamy et al. (2010) [11], reflecting the complexity of spectral evolution and particle acceleration in GPs emission. The single-Gaussian fit yields a mean $\mu = -1.59$ and standard deviation $\sigma = 1.02$, which is in good agreement with the typical spectral index range of classical GPs, $\alpha \approx -1.5$ to -2.0 [21]. The MP–broadband GPs sample mainly occupies the central region of the distribution and overlaps closely with the narrow-window distribution, confirming the robustness of the measurement.

Figure 5(b) shows the spectral index distribution for the interpulse. Due to the limited number of observations, the distribution is relatively sparse and exhibits multiple peaks, with the core range approximately $\alpha \approx -3.2$ to -1.7. The mean spectral index is more negative, reflecting the relative rarity of interpulse emission [22] and consistent with previous findings that the interpulse spectrum is steeper than that of the main pulse [23]. Comparison between the main pulse and interpulse distributions reveals notable differences in both the shape and central spectral index value.These findings should be interpreted with caution, as they may be influenced by the limited sample size as well as intrinsic differences in the emission physics of the two pulse types.

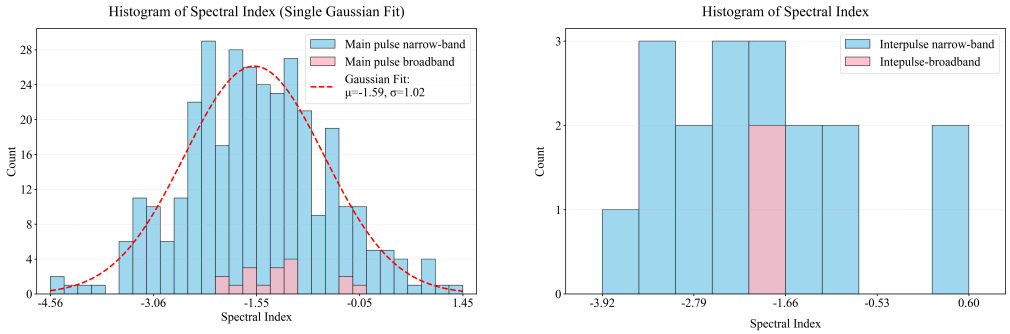

(**a**) (**b**)

Figure 5. Histograms of the spectral indices for GPs in the main pulse and interpulse , shown in panels (a) and (b), respectively. In the plots, the blue histogram represents main pulse GPs, and the pink histogram represents interpulse GPs. The red curve indicates a Gaussian fit to the narrow-band GPs distribution.

 doi:10.20944/preprints202604.1002.v1

3.3. Statistical Analysis of the Giant Pulses Energy Distribution

To investigate the energy statistics of the giant GPs population, we analyzed the relative energy distribution of narrow-band main pulse GPs. Here, the relative energy is defined as $E/\langle E\rangle$, where $\langle E\rangle$ denotes the mean energy of all pulses. Figure 6 shows the histogram of relative energies for narrow-band main pulse, with the horizontal axis representing $E/\langle E\rangle$ and the vertical axis representing the pulse counts in each energy bin.

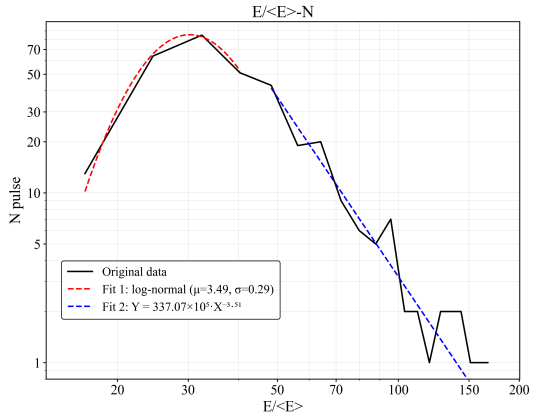

Figure 6. Figure 6 shows the statistical distribution of the relative energy for narrow-band main pulse. The solid black line represents the observational data, while the red dashed line (log-normal distribution) and the blue dashed line (power-law distribution) correspond to the fits from two different models, respectively.

As shown in Figure 6,The energy distribution of the narrow-band MP GPs is broadly consistent with a log-normal form at low-to-intermediate energies and a power-law-like tail at the high-energy end. At lower energies ($E/\langle E\rangle \lesssim 30$), the number of pulses increases rapidly, while at higher energies ($E/\langle E\rangle \gtrsim 30$), the number of pulses decreases. The high-energy tail approximately follows a power-law distribution, though this result should be regarded as a phenomenological description due to the finite sample size and the influence of binning and fitting range on the histogram-based analysis. Given these limitations, the fitted models provide useful guidance for understanding the general behavior of the energy distribution, rather than a definitive statistical decomposition. To quantitatively describe this distribution, both a log-normal distribution and a power-law distribution were fitted to the observed data (Figure 6).

(1) **Log-normal fitting** The red dashed line represents the fit using a log-normal distribution model, with best-fit parameters $\mu = 3.49$ and $\sigma = 0.29$. This model reproduces the overall shape of the observed distribution well in the mid-to-low energy range ($E/\langle E\rangle \lesssim 40$), including the position of the distribution peak and the local statistical features. However, at the high-energy end, the fit systematically deviates from the observed data, indicating that the log-normal model cannot simultaneously describe the high-energy tail.

(2) **Power-law fitting** The blue dashed line represents the power-law model fitted to the high-energy tail, with a power-law index $\alpha = -3.51$. In the high-energy region ($E/\langle E\rangle \gtrsim 40$), the power-law model matches the observed data significantly better than the log-normal model, capturing the rapid decline in GPs counts with increasing energy.

In summary, the energy distribution of narrow-band main pulse GPs exhibits distinct statistical behaviors in the mid-to-low and high-energy ranges: the former is well approximated by a log-normal distribution, while the latter is more consistent with a power-law distribution.

3.4. Statistical Analysis of Giant-Pulse Widths and Their Relation to Signal-to-Noise Ratio

To investigate the temporal characteristics of GPs, we analyzed the time-domain profiles of main pulse events using the 3σ pulse width, defined as the effective duration over which the pulse intensity

 doi:10.20944/preprints202604.1002.v1

exceeds the background noise level by 3σ. This quantity provides a practical measure of the observed temporal extent of each event within the processed single-pulse data.

The distribution of 3σ widths is shown in Figure 7(a). For the narrow-band main pulse sample, the histogram can be empirically described by a double-Gaussian model, with two fitted centroids located near 0.33 ms and 0.41 ms. This fit provides a convenient phenomenological representation of the observed width distribution and suggests the presence of possible clustering within the range of measured widths. However, these fitted components should not be over-interpreted as fully resolved intrinsic width states. The processed data have a time resolution of 128 μs, and each pulsar rotation is divided into 256 phase bins, corresponding to an effective sampling interval of about 0.13 ms per phase bin after folding. Therefore, although the formal uncertainties of the fitted centroids may be small, the effective uncertainty associated with width measurement is limited by the finite time sampling and is of the order of one phase bin. In this sense, the fitted centroids near 0.33 ms and 0.41 ms are better regarded as approximate locations of possible clustering in the histogram rather than as precise measurements of two sharply separated intrinsic timescales. Likewise, the Gaussian widths in the fit reflect the internal description of the histogram model and should not be interpreted directly as the observational resolving power of the dataset. Given these limitations, the apparent bimodal tendency in the narrow-band sample should be considered suggestive rather than conclusive. For the broadband main pulse sample, the measured 3σ widths are more sparsely distributed, roughly between 0.33 and 0.41 ms, and no similarly clear double-peaked structure is evident. Because this subsample is much smaller, the current data do not support a strong comparative conclusion regarding intrinsic differences in temporal structure between narrow-band and broadband events.

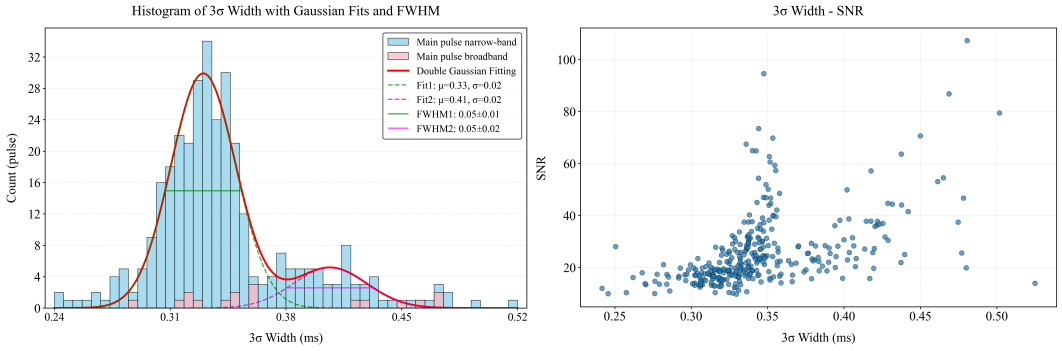

(**a**) (**b**)

Figure 7. (a) Histogram of 3σ widths for main pulse GPs. The red curve shows an empirical double-Gaussian fit to the narrow-band sample, with fitted centroids near 0.33 ms and 0.41 ms. Because the effective sampling interval after folding is about 0.13 ms per phase bin, these fitted components should be interpreted as approximate clustering locations in the observed width distribution rather than fully resolved intrinsic width states. (b) Scatter plot of 3σ width versus signal-to-noise ratio (SNR) for narrow-band main pulse GPs.

To further examine whether pulse width is related to pulse strength, Figure 7(b) shows the scatter plot of 3σ width versus SNR for the main pulse GPs. The SNR values span a broad range, while the widths are mainly distributed between approximately 0.30 and 0.45 ms. Across the observed parameter space, high-SNR events are not confined to a specific width interval, and lower-SNR events are likewise spread across the same width range. This indicates that no strong one-to-one correspondence is evident between pulse width and SNR in the present sample. Although relatively dense regions appear near the fitted centroids, this feature should be interpreted consistently with the finite time resolution discussed above. Overall, the width statistics suggest that narrow-band main pulse GPs may preferentially occupy a limited range of observed durations, with possible substructure in the histogram. However, higher time resolution and a larger sample will be required to determine whether this behavior reflects genuine intrinsic width components or is partly shaped by measurement discretization and finite-sampling effects[6].

 doi:10.20944/preprints202604.1002.v1

3.5. Waiting-Time Statistics of Giant Pulses

To systematically characterize the temporal statistical behavior of GPs from the Crab pulsar, we analyzed the pulse waiting times from three perspectives: the distribution shape, logarithmic-scale properties, and the randomness of the time series.

3.5.1. Waiting-Time Distribution and Weibull Fitting

We first analyzed the waiting times (ΔT) between consecutive GPs. Figure 8 shows the normalized occurrence rate of waiting times as a function of ΔT in a log–log scale. As shown, the occurrence rate decreases monotonically with increasing ΔT, exhibiting a smooth and continuous distribution over several orders of magnitude in timescales. At short timescales ($\Delta T \lesssim 1$ s), the occurrence rate drops rapidly, while at longer timescales ($\Delta T \gtrsim 1$ s), the distribution approximately follows a linear decay in log–log coordinates, though the slope changes.

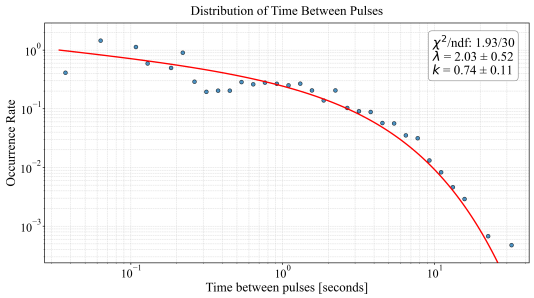

Figure 8. Statistical distribution of waiting times between GPs from the Crab pulsar. The horizontal axis represents the pulse intervals (ΔT), and the vertical axis represents the corresponding occurrence rates, with both axes in logarithmic scale. Blue points indicate the observed data, while the red solid line shows the fit using a Weibull distribution model.

To quantitatively characterize this distribution, we fitted the observed data using a Weibull distribution, whose probability density function is given by:

$$f(t;k,\lambda) = \frac{k}{\lambda}\left(\frac{t}{\lambda}\right)^{k-1} e^{-(t/\lambda)^k}, \tag{2}$$

where t is the waiting time, k is the shape parameter, and λ is the scale parameter. The fit, shown as the red solid line in Figure 8, agrees well with the observed data across the full timescale range.

The best-fit shape parameter is $k = 0.74 \pm 0.11$,indicating that the Weibull function provides a useful empirical description of the observed waiting-time distribution[24,25]. However, this does not by itself establish the presence of deterministic temporal memory or non-random triggering between successive pulses[26]. In the present work, the Weibull fit should be understood primarily as a compact phenomenological model for the waiting-time statistics.

3.5.2. Waiting Time Distribution and Temporal Independence of Giant Pulses

Considering that the waiting time ΔT spans several orders of magnitude, we further analyzed the distribution of $\log_{10} \Delta T$. Figure 9 shows the histogram of $\log_{10} \Delta T$ and its Gaussian fit. The distribution exhibits an approximately symmetric, unimodal shape. Fitting with a Gaussian function yields a mean of $\mu = 0.21 \pm 0.55$ and a standard deviation of $\sigma = 0.55 \pm 0.01$. On the logarithmic timescale, this indicates that GPs waiting times are concentrated around a characteristic interval. Converting back to linear time, the typical waiting time is approximately $10^{\mu} \approx 1.62$ s, with the main distribution range spanning roughly 0.46 s to 5.75 s, reflecting significant statistical dispersion within this scale.

 doi:10.20944/preprints202604.1002.v1

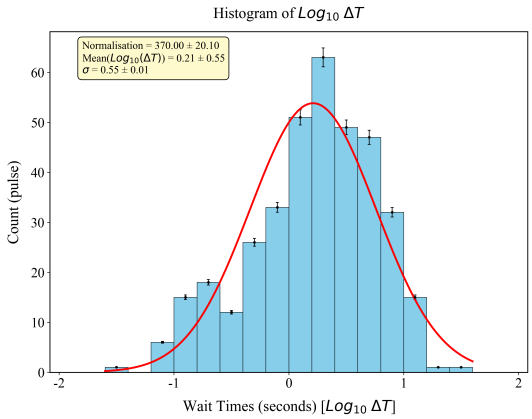

Figure 9. Histogram of the logarithm (base 10) of waiting times (ΔT) between GPs from the Crab pulsar, shown as $\log_{10}\Delta T$. The horizontal axis represents $\log_{10}\Delta T$, and the vertical axis represents the corresponding pulse counts. Blue bars indicate the observed data, while the red solid line shows the Gaussian fit to the distribution.

To explore whether GPs bursts exhibit significant temporal dependence, we performed a sliding-window analysis on the full observation dataset (33,531 pulse periods) and compared it with random Poisson sequences. The window size was set to 1000 pulse periods, with a step size of 200 periods. The burst rate of GPs was calculated within each window, and Figure 10 shows the temporal evolution of the observed burst rate. To assess statistical significance, 1000 random Poisson sequences with the same mean burst rate were generated and subjected to the same sliding-window analysis. In Figure 10, the gray shaded region represents the 95% confidence interval of the random Poisson simulations, the gray dashed line indicates their mean burst rate, and the red horizontal line represents the global mean burst rate of the observed data (0.01). The results indicate that the observed burst rate series almost entirely falls within the 95% confidence interval of the random Poisson simulations and fluctuates around the global mean. Further statistical comparison shows that the variance of the observed series (1.20×10^{-5}) closely matches the mean variance of the simulated Poisson sequences (1.07×10^{-5}), with a Monte Carlo P-value of 0.25, exceeding the 0.05 significance threshold. Thus, we conclude that, within the current observation span of approximately 19 minutes, the GPs burst sequence does not show strong temporal dependence and is statistically indistinguishable from a random Poisson process. However, the apparent lack of temporal correlation may be due to the limited observation duration and sample size, and future studies with longer timescales and higher sensitivity are needed to further investigate potential temporal correlations or "memory effects" in the GPs bursts.

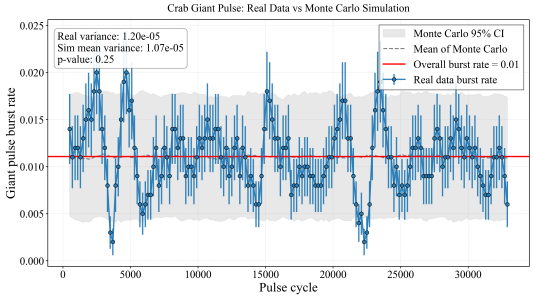

Figure 10. Comparison of the observed burst rate of GPs from the Crab pulsar with Monte Carlo simulated Poisson sequences. The gray shaded region represents the 95% confidence interval of the burst rates derived from 1000 Monte Carlo simulations of random Poisson sequences. The gray dashed line indicates the mean burst rate of the simulated sequences. Blue points with error bars show the observed burst rate and its statistical uncertainty in each sliding window. The red horizontal line represents the global mean burst rate of the observed data over the full observation period (0–33,530 pulse periods), equal to 0.01.

 doi:10.20944/preprints202604.1002.v1

4. Discussion

Using a reproducible empirical classification scheme based on the cumulative distribution function (CDF) of pulse energy, this study distinguishes narrow-band and broadband giant pulses (GPs) under ultra-wideband observing conditions and shows that narrow-band events dominate the present sample. This result supports the view that Crab pulsar GPs do not constitute a single, uniform emission phenomenon, but instead encompass multiple forms of emission with distinct spectral characteristics, in agreement with previous studies of GP energy distributions and spectral behavior [4]. The observed differences in the energy distributions of different GP classes further suggest diversity in the underlying emission processes. In addition, the detection of a large population of narrow-band GPs reinforces earlier evidence for spectral differentiation within the Crab GP population [12]. In the frequency domain, narrow-band GPs concentrate most of their energy within a limited spectral range and exhibit a wide spread of spectral indices, including both negative and positive values. While negative spectral slopes are consistent with the conventional low-frequency-dominated trend, the rare positive slopes depart from this picture and may point to less explored or atypical excitation processes. The relative-bandwidth distribution likewise indicates clear frequency localization and selectivity, highlighting the spectral heterogeneity and complexity of narrow-band GP emission.

These properties are consistent with an origin in localized, frequency-selective coherent emission regions within the pulsar magnetosphere [12], potentially associated with plasma-instability-driven processes such as turbulent wave-packet collapse [4]. Such an interpretation is also compatible with a highly stratified magnetospheric environment, in which emission generated at different heights or under different plasma conditions gives rise to distinct spectral signatures [27]. By contrast, broadband GPs distribute their energy across a much wider frequency range, and their spectra are generally not well described by a single power-law model [11,23]. This behavior suggests a more complex emission picture, possibly involving multiple overlapping components or large-scale coherent structures capable of radiating efficiently over broad frequency intervals. Previous work has likewise shown that Crab GPs can display broadband characteristics and broad spectral-index distributions that are difficult to explain within a single unified framework [9,11]. Therefore, the spectral contrast between narrow-band and broadband GPs lends further support to the idea that multiple emission components or mechanisms may coexist in the Crab pulsar. In this respect, the phenomenological distinction between the two classes may also offer a useful point of comparison with the diversity observed in narrow-band and broadband fast radio bursts (FRBs) [28]. Overall, the systematic spectral differences identified here provide additional observational constraints for evaluating multi-component or multi-mechanism models of GP emission and help clarify the possible physical origins of these two classes.

The high-energy tail of the narrow-band main pulse energy distribution, at $E/\langle E\rangle > 40$, shows an approximate power-law behavior with an index of about -3.51. Scale-free tails of this kind are common in complex systems and are often associated with nonlinear amplification or cross-scale energy-release processes [14], suggesting that the strongest GPs are not governed by a single characteristic energy scale. Instead, they may arise from episodic energy release when magnetospheric conditions approach a critical state, with event sizes spanning a broad dynamic range [29,30]. At the same time, the good agreement between the mid-to-low-energy part of the distribution and a log-normal form may reflect the combined influence of multiple stochastic factors in the buildup or modulation of the radiated energy [6,7]. Taken together, these results suggest that the energy statistics of narrow-band main pulse GPs may encode contributions from more than one physical regime, although the limited sample size and the histogram-based fitting procedure mean that this interpretation should remain phenomenological at the present stage.

The 3σ pulse-width distribution of narrow-band main pulse GPs shows two apparent concentrations near 0.33 ms and 0.41 ms, with neither component exhibiting a strong dependence on signal-to-noise ratio (SNR). This may indicate that pulse width is a more intrinsic observational characteristic than peak intensity and may be linked more directly to the characteristic timescale of the emission process [7,11]. Narrower events could correspond to smaller or more coherent emission regions whose

 doi:10.20944/preprints202604.1002.v1

temporal extent is constrained by local physical conditions, such as the geometric scale or coherence length of the emitting region [31]. Slightly broader events, on the other hand, may reflect lateral expansion of the emitting region, propagation effects, or instabilities operating on somewhat different characteristic scales [32–34]. However, this interpretation should be treated with caution because the effective time sampling of the present data is limited, and the apparent bimodality may be influenced in part by finite time resolution and measurement discretization.

The waiting-time analysis shows that GP intervals are well described empirically by a Weibull distribution with shape parameter $k < 1$, indicating a form that differs from a simple exponential law [24,25]. However, the sliding-window analysis and Monte Carlo comparisons show that, over the approximately 19-minute observing span, the observed burst sequence is statistically indistinguishable from a temporally independent Poisson process [25,35]. Thus, the current dataset does not provide strong evidence for significant temporal correlations or deterministic memory effects in the GP sequence [11]. The apparent tension between the Weibull-like waiting-time distribution and the Poisson-consistent burst-rate fluctuations may arise from a combination of limited observing duration, finite sample size, and selection or threshold effects. Longer observations with improved sensitivity will be needed to determine more reliably whether Crab GPs exhibit genuine temporal correlations on particular timescales.

5. Conclusions

Based on Parkes UWL observations, we have carried out a phenomenological analysis of the spectral, temporal, and statistical properties of giant pulses from the Crab pulsar. The main results can be summarized as follows:

1. Using the cumulative distribution function of pulse energy in frequency, we introduce a reproducible empirical scheme to describe the spectral extent of individual GPs. Under this scheme, 353 events are classified as narrow-band and 19 as broadband, indicating that narrow-band events dominate the present sample.
2. The spectral indices of narrow-band MP GPs cover a broad range, with most events showing negative slopes and a few showing positive slopes. This indicates substantial spectral diversity within the observed sample, although detailed physical interpretation requires caution because no absolute flux calibration is available.
3. The 3σ widths of narrow-band MP GPs show two apparent concentrations near 0.33 ms and 0.41 ms. At the current time resolution, this feature is best regarded as suggestive of possible preferred width ranges rather than conclusive evidence for discrete intrinsic timescales.
4. The energy distribution of narrow-band MP GPs is broadly consistent with a log-normal form at lower energies and a power-law-like tail at higher energies, providing a useful empirical description of the sample.
5. The waiting-time distribution can be described by a Weibull function, while the burst-rate fluctuations over the 18.9-minute observing span are statistically consistent with a Poisson-like process. Taken together, these results do not provide strong evidence for temporal memory in the present dataset.

Overall, this work provides a wideband observational description of Crab giant pulses and highlights several trends that merit further investigation with longer observations, larger samples, improved calibration, and higher time resolution.

Author Contributions: Author Contributions: Conceptualization, R.Z. and H.L.; methodology, R.Z.; software, L.W., R.Z. and H.L.; validation, L.W.; formal analysis, Z.T.,H.X. and R.T.; investigation, R.T. and Q.Z.; resources, R.Z. and H.L.; data curation, L.W.; writing–original draft preparation,L.W. and R.Z.; writing–review and editing, L.W.,R.Z.,H.L. and D.Y.; visualization, L.W.,K.Y.,J.F. and Y.Z.; supervision, R.Z. and H.L.; project administration, R.Z. and H.L. All authors have read and agreed to the published version of the manuscript.

 doi:10.20944/preprints202604.1002.v1

Funding: We gratefully acknowledge support from the following agencies and programs: National Natural Science Foundation of China (Grant Nos. 12563008, 11988101, U1731238, U2031117, 11565010, 11725313, 1227308, 12041303, 12588202); National Key R&D Program of China (No. 2023YFE0110500); National SKA Program of China (Nos. 2020SKA0120200, 2022SKA0130100, 2022SKA0130104); Science and Technology Foundation of Guizhou Provincial Department of Education (No. KY(2023)059); Youth Innovation Promotion Association CAS (ID: 2021055); Youth Scientists Project of Basic Research in CAS (YSBR-006); Foreign Talents Program (No. QN2023061004L; E.G.); Scientific and Technological Innovation Team of Higher Education Institutions under the Education Department of Guizhou Province (Grant No. QJJ[2023]093); Natural Science Research Support Project of the Education Department of Guizhou Province (No. [2024]350, KY[2018]006); CAS Youth Interdisciplinary Team; Liupanshui Science and Technology Development Project (No. 52020-2024-PT-01); the Cultivation Project for FAST Scientific Payoff and Research Achievement of CAMS-CAS. P.W. acknowledges additional support from the CAS Youth Interdisciplinary Team, the Youth Innovation Promotion Association CAS, and the Cultivation Project for FAST Scientific Payoff and Research Achievement of CAMS-CAS. D.L. is supported as a New Cornerstone Investigator. These supports were instrumental in the successful completion of this work.

Data Availability Statement: The data that support the findings of this study are available from the corresponding author upon reasonable request.

Acknowledgments: The authors would like to express their sincere gratitude to [Name] for insightful discussions and valuable support throughout this study. During the preparation of this manuscript, artificial intelligence tools were employed to assist in the translation of content. All outputs generated with the assistance of artificial intelligence were carefully reviewed, refined, and edited by the authors, who take full responsibility for the final manuscript.

Conflicts of Interest: The authors declare no conflict of interest. The funders had no role in the design of the study; in the collection, analyses, or interpretation of data; in the writing of the manuscript; or in the decision to publish the results.

Appendix A

Appendix A.1

Table A1 presents the measured parameters of identified giant pulses, including normalized pulse energy ($E/<E>$), signal-to-noise ratio (SNR), central frequency (ν_c), bandwidth (BW), relative bandwidth (BW/ν_c), and spectral index (α). The table includes all four categories: MP-Narrow-band, MP-broadband, IP-Narrow-band, and IP-broadband.

Table A1. Parameters of Identified Giant Pulses.

Number	$E/<E>$	SNR	Vc(MHz)	BW(MHz)	BW/Vc	α
MP-Narrow-band						
19	29.64	15.57	1333.50	873.00	0.65	-1.52±0.35
60	79.27	70.65	1643.50	1493.00	0.91	-0.95±0.23
79	29.24	16.93	1355.00	916.00	0.68	-2.41±1.17
139	54.12	28.02	1410.00	1026.00	0.73	-0.21±0.47
163	27.05	13.34	1281.50	769.00	0.60	-1.38±0.25
171	15.59	12.03	1442.00	1090.00	0.76	-1.37±0.41
207	22.73	15.74	1412.50	1031.00	0.73	-0.90±0.28
254	59.88	32.27	1359.00	924.00	0.68	-1.18±0.87
446	41.82	18.32	1246.00	698.00	0.56	-1.44±1.02
648	47.12	28.49	1443.50	1093.00	0.76	-0.81±0.51
749	28.27	20.35	1492.50	1191.00	0.80	-2.11±0.32
998	24.16	16.67	1491.50	1189.00	0.80	-0.77±0.26
1013	16.15	10.36	1471.50	1149.00	0.78	-1.62±0.48
1042	40.44	19.04	1292.00	790.00	0.61	0.19±0.36
1144	34.19	19.40	1308.50	823.00	0.63	-3.14±0.85

 doi:10.20944/preprints202604.1002.v1

1277	18.89	14.12	1558.50	1323.00	0.85	-1.17±0.45
1308	73.96	38.26	1422.50	1051.00	0.74	-1.18±0.34
1335	55.43	37.01	1415.00	1036.00	0.73	-1.48±0.51
1447	30.72	14.60	1405.00	1016.00	0.72	-0.99±0.41
1449	49.25	10.21	1009.00	224.00	0.22	0.27
1544	15.62	9.76	1318.50	843.00	0.64	-3.24±0.71
1656	83.77	54.51	1475.50	1157.00	0.78	-2.33±0.25
1804	24.60	19.01	1545.50	1297.00	0.84	-0.89±0.15
1873	21.09	13.41	1321.50	849.00	0.64	-2.70±0.63
1890	27.10	12.32	1307.00	820.00	0.63	-0.66±0.38
2019	64.07	37.27	1567.00	1340.00	0.86	-2.33±0.76
2023	52.38	29.07	1462.00	1130.00	0.77	-0.82±0.58
2034	30.24	17.13	1350.50	907.00	0.67	-0.23±0.23
2102	35.94	19.82	1374.50	955.00	0.69	-2.60±0.51
2171	23.59	14.98	1371.50	949.00	0.69	-1.21±0.69
2244	48.09	31.45	1516.00	1238.00	0.82	-1.40±0.24
2274	81.96	45.03	1357.00	920.00	0.68	-0.08±0.26
2341	33.47	15.52	1284.00	774.00	0.60	-3.80±0.42
2342	39.38	27.46	1514.50	1235.00	0.82	-0.37±0.17
2408	26.05	15.42	1489.00	1184.00	0.80	-0.56±0.44
2548	73.95	41.54	1431.00	1068.00	0.75	-1.00±0.30
2679	39.72	19.92	1338.00	882.00	0.66	0.59±0.46
2689	52.56	30.04	1387.50	981.00	0.71	-1.97±0.45
2713	84.13	49.85	1324.00	854.00	0.65	-1.13±0.75
2785	62.46	39.09	1520.00	1246.00	0.82	-0.90±0.19
2833	27.64	15.73	1457.00	1120.00	0.77	-1.12±0.34
2899	94.40	62.72	1427.50	1061.00	0.74	-0.42±0.59
2905	57.72	29.93	1428.00	1062.00	0.74	-1.10±0.58
2945	68.96	36.55	1319.00	844.00	0.64	-3.01±0.49
2990	24.65	17.17	1422.00	1050.00	0.74	-2.88±0.58
3006	60.65	36.30	1410.00	1026.00	0.73	-1.73±0.36
3077	46.21	23.51	1412.50	1031.00	0.73	-1.73±0.53
3087	39.29	27.34	1432.50	1071.00	0.75	-0.20±0.60
4125	28.06	16.63	1369.50	945.00	0.69	-2.50±1.14
4160	29.16	19.61	1376.00	958.00	0.70	-1.54±0.42
4209	31.04	19.91	1384.50	975.00	0.70	-1.98±0.10
4241	20.52	16.20	1437.50	1081.00	0.75	-2.13±0.43
4253	23.37	12.72	1327.50	861.00	0.65	-1.43±0.67
4275	20.18	9.95	1152.50	511.00	0.44	0.85±2.18
4279	32.11	23.66	1503.50	1213.00	0.81	-1.15±0.34
4292	34.36	21.65	1432.00	1070.00	0.75	-1.68±0.83
4442	30.39	14.50	1320.00	846.00	0.64	-1.84±0.65
4587	36.57	21.26	1364.00	934.00	0.68	-0.81±0.63
4618	32.54	18.59	1503.00	1212.00	0.81	-2.29±0.27
4631	51.40	29.35	1345.50	897.00	0.67	-2.28±0.37
4696	22.57	14.00	1359.00	924.00	0.68	-0.97±1.14
4699	33.10	21.27	1447.00	1100.00	0.76	-1.46±0.25
4852	31.70	18.04	1328.50	863.00	0.65	-1.91±0.47
4885	63.65	29.00	1319.50	845.00	0.64	-1.72±0.77
4903	29.15	13.54	1268.50	743.00	0.59	-2.05±0.93

 doi:10.20944/preprints202604.1002.v1

4995	45.37	23.21	1450.00	1106.00	0.76	-0.38±0.44
5022	45.19	25.40	1316.00	838.00	0.64	-3.48±0.48
5071	49.63	27.55	1398.00	1002.00	0.72	-1.13±0.63
5075	16.77	10.37	1313.50	833.00	0.63	-1.43±0.90
5315	16.39	13.28	1633.50	1473.00	0.90	-1.00±0.14
5333	57.54	31.33	1280.50	767.00	0.60	-1.28±0.24
5402	42.04	24.25	1414.50	1035.00	0.73	-2.49±0.21
5420	37.78	20.57	1390.00	986.00	0.71	-1.89±0.85
6335	38.52	22.06	1383.00	972.00	0.70	-1.08±0.29
6461	22.94	14.79	1578.00	1362.00	0.86	-1.42±0.43
6483	30.06	20.40	1436.00	1078.00	0.75	-1.34±0.28
6507	29.13	17.39	1346.50	899.00	0.67	-2.19±0.83
6515	48.33	25.67	1326.50	859.00	0.65	-0.06±0.22
6779	12.65	10.02	1667.50	1541.00	0.92	-1.67±0.24
6988	19.88	11.03	1333.50	873.00	0.65	-0.01±0.31
7026	55.72	23.75	1317.50	841.00	0.64	-1.12±0.43
7039	34.23	21.00	1437.00	1080.00	0.75	-1.81±0.52
7243	56.71	30.04	1390.00	986.00	0.71	-2.31±0.53
7291	31.78	17.15	1302.00	810.00	0.62	-2.19±0.52
7355	34.52	29.58	1700.00	1606.00	0.94	-1.83±0.43
7708	63.35	44.42	1502.00	1210.00	0.81	-1.65±0.30
7798	23.56	13.59	1367.50	941.00	0.69	-1.05±0.49
7852	91.85	50.14	1479.50	1165.00	0.79	-0.58±0.47
7893	21.66	13.43	1385.00	976.00	0.70	-2.66±0.40
7956	21.46	13.35	1539.00	1284.00	0.83	-1.03±0.35
7972	21.50	13.86	1340.00	886.00	0.66	-2.50±0.39
8057	36.77	22.96	1370.00	946.00	0.69	-1.53±0.61
8187	47.63	27.06	1393.50	993.00	0.71	-2.30±0.30
8359	30.47	16.43	1348.50	903.00	0.67	-1.64±0.52
8428	33.44	12.48	1122.00	450.00	0.40	0.58±0.27
8505	38.95	27.05	1432.50	1071.00	0.75	-1.88±0.19
8528	29.00	18.73	1410.50	1027.00	0.73	-3.17±0.30
8535	38.59	18.80	1257.00	720.00	0.57	-3.19±0.94
8567	92.92	54.32	1372.00	950.00	0.69	-2.32±0.53
8607	45.23	24.48	1406.50	1019.00	0.72	-1.76±0.14
8753	43.71	25.51	1367.00	940.00	0.69	-1.71±0.38
8887	31.25	17.84	1538.00	1282.00	0.83	-1.38±0.20
8890	36.04	21.07	1279.00	764.00	0.60	-3.12±0.75
9060	46.66	31.25	1542.00	1290.00	0.84	-1.71±0.58
9092	27.22	13.21	1324.50	855.00	0.65	-2.09±0.52
9141	24.94	16.98	1474.00	1154.00	0.78	-0.45±0.46
9396	35.33	25.15	1487.50	1181.00	0.79	-1.84±0.23
9532	24.93	16.67	1604.50	1415.00	0.88	-0.56±0.47
9615	35.79	18.77	1397.50	1001.00	0.72	-0.92±0.47
9633	22.41	28.07	1857.00	1920.00	1.03	-1.31±0.48
9790	34.18	20.79	1309.50	825.00	0.63	-2.01±0.17
9830	34.54	19.12	1310.00	826.00	0.63	-1.77±0.87
9886	139.77	86.81	1330.50	867.00	0.65	-1.74±0.37
10064	34.32	18.28	1326.50	859.00	0.65	-1.52±0.36
10350	26.68	16.65	1375.50	957.00	0.70	-2.63±0.87

 doi:10.20944/preprints202604.1002.v1

10368	65.25	31.75	1403.00	1012.00	0.72	-1.34±0.18
10373	30.59	18.72	1416.50	1039.00	0.73	-1.83±0.50
10432	60.88	37.45	1326.00	858.00	0.65	-2.03±0.38
10450	49.60	26.86	1357.50	921.00	0.68	-1.42±0.37
10496	26.76	18.72	1410.00	1026.00	0.73	-1.78±0.60
10721	30.83	15.84	1328.50	863.00	0.65	-1.30±0.50
10725	25.67	19.13	1664.00	1534.00	0.92	-0.30±0.47
10841	28.30	14.84	1291.00	788.00	0.61	-3.13±0.48
10958	39.81	28.22	1511.00	1228.00	0.81	-2.91±0.27
10970	37.86	17.18	1258.00	722.00	0.57	-2.30±0.70
11071	67.25	40.08	1388.00	982.00	0.71	-1.80±0.22
11096	17.45	12.84	1687.00	1580.00	0.94	-1.88±0.31
11102	39.72	25.78	1492.00	1190.00	0.80	-0.89±0.38
11138	24.24	13.25	1338.50	883.00	0.66	-4.22±0.32
11335	26.28	13.60	1328.50	863.00	0.65	-2.65±1.37
11419	34.87	22.49	1458.50	1123.00	0.77	-1.95±0.22
11521	96.42	53.04	1333.00	872.00	0.65	-2.34±0.46
11624	38.46	23.34	1353.50	913.00	0.67	-2.07±0.40
11650	49.16	27.55	1510.50	1227.00	0.81	-0.59±0.46
11842	22.39	11.28	1317.50	841.00	0.64	-2.95±0.11
11950	91.97	46.76	1460.50	1127.00	0.77	-1.86±0.39
11989	51.59	28.27	1308.00	822.00	0.63	-1.92±0.32
12052	62.80	28.43	1326.50	859.00	0.65	-2.68±0.76
12434	31.94	17.15	1349.00	904.00	0.67	-3.13±0.96
12476	37.85	17.22	1369.50	945.00	0.69	-0.86±0.98
12505	37.57	21.85	1316.50	839.00	0.64	-1.62±0.41
12520	38.24	26.32	1558.50	1323.00	0.85	-1.74±0.54
12841	52.62	35.05	1483.00	1172.00	0.79	-0.76±0.18
12911	28.46	17.35	1433.00	1072.00	0.75	-1.71±0.39
12955	60.12	35.80	1392.50	991.00	0.71	-1.74±0.32
12968	49.08	21.92	1324.50	855.00	0.65	-3.35±0.57
13034	64.67	44.64	1449.50	1105.00	0.76	-1.74±0.20
13036	45.54	23.35	1323.50	853.00	0.64	-2.64±0.86
13174	43.68	25.59	1455.50	1117.00	0.77	-2.25±0.50
13285	43.84	14.79	1118.00	442.00	0.40	-3.14±3.18
13463	51.68	30.71	1415.50	1037.00	0.73	-1.09±0.18
13710	27.99	16.60	1430.50	1067.00	0.75	-2.98±0.24
13821	46.49	23.49	1317.50	841.00	0.64	-4.12±0.43
14333	26.68	12.92	1400.50	1007.00	0.72	-0.45±0.37
14379	119.03	79.46	1496.00	1198.00	0.80	-1.21±0.36
14778	33.22	20.56	1333.50	873.00	0.65	-0.77±0.35
14878	69.15	31.87	1302.00	810.00	0.62	-4.37±0.94
14931	75.13	33.90	1311.00	828.00	0.63	-1.3±0.79
15107	40.33	24.05	1302.50	811.00	0.62	-1.27±0.85
15112	60.39	37.85	1315.50	837.00	0.64	-2.43±0.38
15160	32.46	22.62	1458.50	1123.00	0.77	-1.24±0.27
15274	46.59	28.99	1496.00	1198.00	0.80	-0.42±0.42
15285	27.62	21.12	1341.00	888.00	0.66	-0.77±0.46
15288	32.22	17.44	1366.00	938.00	0.69	-0.24±0.67
15322	24.22	15.83	1457.50	1121.00	0.77	-2.47±0.29

 doi:10.20944/preprints202604.1002.v1

15333	37.65	19.94	1414.50	1035.00	0.73	-0.45±0.41
15356	29.95	20.74	1446.00	1098.00	0.76	-0.38±0.40
15397	61.57	37.45	1415.50	1037.00	0.73	-2.26±0.36
15422	26.88	17.53	1344.00	894.00	0.67	-2.53±0.20
15462	40.59	18.93	1244.50	695.00	0.56	-1.71±0.94
15498	86.32	46.73	1321.50	849.00	0.64	-1.24±0.75
15565	86.02	59.33	1490.00	1186.00	0.80	-2.46±0.51
15861	32.53	12.36	1184.50	575.00	0.49	-2.00±0.50
16098	43.49	25.84	1328.00	862.00	0.65	-0.14±0.52
16210	109.10	63.64	1334.50	875.00	0.66	-2.72±0.34
16240	94.69	46.97	1424.50	1055.00	0.74	0.14±0.55
16266	48.44	24.53	1327.50	861.00	0.65	-1.19±0.65
16284	35.16	21.92	1419.50	1045.00	0.74	-0.23±0.26
16291	40.35	23.37	1391.50	989.00	0.71	-1.55±0.65
16335	46.82	27.95	1496.00	1198.00	0.80	-0.42±0.44
16357	36.42	24.55	1457.50	1121.00	0.77	-0.90±0.31
16431	58.58	31.51	1362.00	930.00	0.68	-0.11±0.41
16744	32.32	19.37	1366.00	938.00	0.69	-1.39±0.43
16834	38.79	26.33	1523.00	1252.00	0.82	-0.20±0.59
17130	24.02	17.43	1358.00	922.00	0.68	-2.52±0.43
17187	32.97	17.24	1312.00	830.00	0.63	-3.44±0.70
17330	45.29	30.86	1434.00	1074.00	0.75	-2.37±0.38
17555	32.74	18.87	1423.50	1053.00	0.74	-1.82±0.35
17558	43.55	29.37	1507.50	1221.00	0.81	-1.23±0.36
17617	24.85	16.34	1320.00	846.00	0.64	-0.20±0.71
17676	21.36	19.52	1684.00	1574.00	0.93	-0.43±0.35
17819	81.78	43.92	1316.00	838.00	0.64	-0.78±0.67
17980	25.70	15.18	1350.00	906.00	0.67	-3.33±0.79
17985	27.00	16.17	1479.00	1164.00	0.79	-2.81±0.36
18094	31.42	17.72	1319.00	844.00	0.64	-3.05±0.87
18313	24.99	16.63	1452.50	1111.00	0.76	-1.08±0.75
18343	26.85	15.00	1406.00	1018.00	0.72	-2.31±0.82
18512	20.69	16.06	1616.00	1438.00	0.89	-0.54±0.39
18570	28.24	20.13	1463.00	1132.00	0.77	-0.78±0.41
18814	26.68	14.72	1338.00	882.00	0.66	0.84±0.61
18883	36.05	26.72	1503.00	1212.00	0.81	-2.11±0.46
18922	47.68	27.48	1451.50	1109.00	0.76	-0.97±0.23
19237	24.09	16.89	1459.00	1124.00	0.77	-1.03±0.68
19299	31.49	17.66	1391.00	988.00	0.71	-1.86±0.67
19453	31.41	18.32	1325.00	856.00	0.65	-2.25±0.95
19513	35.54	22.49	1481.50	1169.00	0.79	-1.55±0.46
19639	91.67	60.59	1449.50	1105.00	0.76	-2.52±0.50
19761	33.03	19.00	1341.50	889.00	0.66	0.32±0.42
19829	35.63	16.38	1336.00	878.00	0.66	-1.83±0.62
19881	32.72	18.42	1343.00	892.00	0.66	-2.17±0.79
19911	28.37	18.73	1453.50	1113.00	0.77	-0.05±0.28
19941	148.91	57.29	1207.00	620.00	0.51	-0.35±0.22
20113	34.62	23.45	1446.50	1099.00	0.76	-1.88±0.19
20287	59.61	40.24	1528.00	1262.00	0.83	-0.98±0.59
20322	35.80	22.32	1354.50	915.00	0.68	-0.96±0.79

 doi:10.20944/preprints202604.1002.v1

20404	23.55	15.87	1547.50	1301.00	0.84	-0.33±0.12
20465	29.19	18.42	1423.00	1052.00	0.74	-1.76±0.56
20481	50.91	28.44	1346.50	899.00	0.67	-1.36±0.31
20556	32.03	16.45	1440.50	1087.00	0.75	-0.10±0.18
20626	60.81	38.20	1391.50	989.00	0.71	-0.39±0.30
20628	19.63	13.38	1572.50	1351.00	0.86	-1.53±0.42
20647	38.13	16.86	1244.00	694.00	0.56	1.45±0.22
20921	88.43	48.51	1457.50	1121.00	0.77	-2.34±0.59
20981	27.37	13.86	1352.50	911.00	0.67	-0.62±0.63
20988	53.26	26.95	1393.00	992.00	0.71	-1.62±0.91
21010	29.59	17.90	1330.50	867.00	0.65	-2.40±0.16
21321	58.98	31.80	1374.00	954.00	0.69	-3.27±0.46
21370	74.08	44.09	1373.00	952.00	0.69	-1.73±0.55
21695	20.19	17.99	1559.00	1324.00	0.85	-1.33±0.47
21710	36.22	15.48	1309.50	825.00	0.63	-1.17±0.32
21795	37.21	25.81	1691.00	1588.00	0.94	-1.45±0.32
21913	40.92	24.41	1403.00	1012.00	0.72	-1.61±0.30
22813	25.35	15.73	1326.00	858.00	0.65	-2.70±0.81
22944	49.15	30.45	1314.00	834.00	0.63	-2.05±1.08
23011	30.75	19.69	1312.50	831.00	0.63	-3.47±0.29
23025	29.97	19.80	1455.00	1116.00	0.77	0.08±0.12
23317	26.02	13.26	1335.00	876.00	0.66	-3.32±0.32
23320	36.19	19.15	1422.00	1050.00	0.74	-1.89±0.59
23322	23.35	15.26	1364.50	935.00	0.69	-2.61±0.11
23326	38.81	13.95	1294.50	795.00	0.61	-2.31±0.55
23330*	9.89	9.89	1307.50	821.00	0.63	-2.53±0.78
23333	42.27	25.02	1318.00	842.00	0.64	-1.73±1.00
23431	55.16	34.74	1397.00	1000.00	0.72	-2.48±0.28
23457	49.37	25.79	1315.00	836.00	0.64	-1.80±0.17
23514	26.53	17.47	1590.00	1386.00	0.87	-2.27±0.40
23571	44.54	28.89	1472.00	1150.00	0.78	0.11±0.21
23574	34.59	20.07	1355.00	916.00	0.68	0.28±0.25
23658	23.71	15.82	1645.00	1496.00	0.91	-2.22±0.44
23727	48.28	28.38	1321.00	848.00	0.64	-3.20±0.72
23917	29.54	17.20	1418.50	1043.00	0.74	-0.40±0.32
23919	26.08	17.49	1316.50	839.00	0.64	-1.08±0.21
24347	61.17	34.00	1284.00	774.00	0.60	-2.42±0.33
24406	49.20	26.01	1397.00	1000.00	0.72	-1.69±0.40
24583	94.80	57.18	1343.50	893.00	0.66	-0.60±0.40
24632	38.86	22.24	1338.00	882.00	0.66	-2.22±0.32
24653	35.70	24.79	1516.00	1238.00	0.82	-1.52±0.31
25102	57.44	33.68	1398.50	1003.00	0.72	0.11±0.56
25138	50.97	34.74	1417.50	1041.00	0.73	-2.25±0.42
25334	31.98	13.77	1318.00	842.00	0.64	-2.28±0.77
25487	33.04	16.61	1302.00	810.00	0.62	-0.92±0.78
25566	27.51	16.93	1424.50	1055.00	0.74	-0.46±0.52
25673	29.84	15.90	1315.00	836.00	0.64	-0.76±0.35
25861	66.56	32.63	1395.50	997.00	0.71	-2.47±0.35
26051	72.08	39.90	1471.50	1149.00	0.78	-2.00±0.32
26135	58.74	31.66	1437.00	1080.00	0.75	-1.07±0.43

 doi:10.20944/preprints202604.1002.v1

26175	28.09	15.19	1429.00	1064.00	0.74	-1.41±0.30
26265	34.66	17.54	1222.00	650.00	0.53	-4.56±0.66
26369	35.82	16.90	1235.50	677.00	0.55	-2.95±0.37
26377	44.52	21.72	1264.50	735.00	0.58	-3.44±0.49
26504	48.78	24.68	1409.50	1025.00	0.73	-2.12±0.42
26512	36.28	22.28	1358.50	923.00	0.68	-2.01±0.72
26748	34.62	14.38	1169.00	544.00	0.47	0.92±0.78
26798	37.42	22.68	1358.50	923.00	0.68	-0.83±0.45
27109	25.36	10.44	1235.50	677.00	0.55	1.04±0.72
27209	102.55	51.86	1336.00	878.00	0.66	-0.11±0.67
27286	77.81	46.90	1410.50	1027.00	0.73	-1.85±0.54
27528	34.74	24.93	1464.50	1135.00	0.78	-0.80±0.36
27550	67.16	42.11	1443.00	1092.00	0.76	-1.27±0.35
27583	46.57	27.68	1479.50	1165.00	0.79	-1.74±0.21
27704	37.67	22.49	1432.00	1070.00	0.75	-0.39±0.35
27744	39.18	21.75	1391.00	988.00	0.71	-2.49±0.90
27833	46.88	31.20	1405.50	1017.00	0.72	-2.16±0.61
27838	33.26	19.15	1373.50	953.00	0.69	-2.44±0.42
27921	66.86	37.56	1330.00	866.00	0.65	-1.80±0.83
28033	38.12	21.53	1305.00	816.00	0.63	-0.54±0.54
28303	32.86	22.21	1396.00	998.00	0.71	-2.47±0.44
28368	50.47	24.11	1317.50	841.00	0.64	-2.22±1.06
28620	40.52	16.41	1171.50	549.00	0.47	-2.98±0.27
28772	35.62	22.04	1411.00	1028.00	0.73	-3.04±0.36
28781	32.84	18.72	1353.50	913.00	0.67	-2.31±0.36
28820	33.94	18.53	1384.00	974.00	0.70	-2.27±0.51
28838	38.75	20.03	1308.50	823.00	0.63	-2.66±0.62
28943	33.39	20.36	1328.50	863.00	0.65	-3.26±1.04
28948	104.97	64.86	1488.00	1182.00	0.79	-2.14±0.21
29047	125.17	64.94	1493.00	1192.00	0.80	-0.37±0.45
29053	40.11	23.86	1501.50	1209.00	0.81	-1.05±0.16
29058	171.03	107.28	1466.50	1139.00	0.78	-1.88±0.34
29061	43.28	20.29	1310.00	826.00	0.63	-2.9±0.80
29344	72.79	39.58	1321.00	848.00	0.64	-2.19±0.24
29520	46.41	30.11	1341.50	889.00	0.66	-1.15±0.33
29574	37.66	18.70	1411.50	1029.00	0.73	0.52±0.34
29580	113.03	69.79	1479.00	1164.00	0.79	-0.38±0.47
29681	64.88	38.69	1355.00	916.00	0.68	-2.52±0.42
29736	49.34	25.78	1410.50	1027.00	0.73	-1.63±0.47
29928	61.79	37.78	1413.50	1033.00	0.73	-3.26±0.89
30030	42.50	23.57	1427.50	1061.00	0.74	-1.84±0.22
30144	57.72	36.62	1402.00	1010.00	0.72	-2.42±0.47
30184	41.02	27.10	1470.00	1146.00	0.78	0.29±0.51
30275	34.87	16.04	1273.00	752.00	0.59	-3.38±0.87
30364	126.52	73.47	1466.50	1139.00	0.78	-2.37±0.26
30450	34.37	19.27	1427.00	1060.00	0.74	-1.00±0.46
30473	23.86	10.71	1406.00	1018.00	0.72	0.01±0.23
30631	33.68	19.85	1405.00	1016.00	0.72	-1.75±0.60
30878	25.74	19.24	1503.00	1212.00	0.81	-1.16±0.50
30898	40.55	22.93	1331.50	869.00	0.65	-1.04±0.22

 doi:10.20944/preprints202604.1002.v1

30933	38.81	24.22	1358.50	923.00	0.68	0.97±0.40
31002	46.66	27.81	1514.00	1234.00	0.82	-0.99±0.42
31338	72.90	37.63	1401.00	1008.00	0.72	0.36±0.45
31360	27.48	17.94	1460.00	1126.00	0.77	1.09±1.40
31592	36.33	14.48	1160.00	526.00	0.45	0.48±1.00
31809	45.03	25.52	1316.50	839.00	0.64	-2.06±0.24
31965	60.25	37.81	1340.50	887.00	0.66	-1.26±0.48
31994	44.95	25.41	1326.00	858.00	0.65	-3.21±0.44
32023	24.46	12.96	1343.50	893.00	0.66	-1.85±1.34
32032	34.43	19.53	1351.50	909.00	0.67	-0.04±0.34
32093	43.79	29.46	1352.50	911.00	0.67	-1.54±0.41
32298	83.81	44.70	1346.00	898.00	0.67	-1.57±0.60
32304	27.94	14.92	1353.00	912.00	0.67	-1.19±0.88
32350	44.83	28.31	1294.00	794.00	0.61	-2.31±0.63
32374	33.22	13.76	1260.50	727.00	0.58	-3.52±1.76
32450	141.02	67.46	1336.00	878.00	0.66	-0.68±0.73
32859	158.16	94.59	1525.50	1257.00	0.82	-1.11±0.26
32949	32.75	22.60	1501.50	1209.00	0.81	-0.48±0.60
33168	38.05	21.76	1446.00	1098.00	0.76	-0.65±0.19
33367	48.13	36.10	1384.00	974.00	0.70	-1.25±0.31
			MP-broadband			
4777	32.54	40.47	2382.00	2970.00	1.25	-1.57±0.18
5483	21.42	31.92	2382.00	2970.00	1.25	-1.19±0.19
10039	71.93	73.61	2382.00	2970.00	1.25	-1.84±0.13
11797	124.24	147.00	2382.00	2970.00	1.25	-1.45±0.15
12411	42.27	46.80	2382.00	2970.00	1.25	-2.07±0.25
13694	115.79	140.49	2382.00	2970.00	1.25	-0.24±0.18
13869	25.16	28.30	2382.00	2970.00	1.25	-1.11±0.23
18626	27.03	25.38	2382.00	2970.00	1.25	-0.27±0.12
20995	84.19	102.89	2382.00	2970.00	1.25	-1.72±0.19
21017	35.08	38.51	2382.00	2970.00	1.25	-1.19±0.20
23087	10.74	14.14	2382.00	2970.00	1.25	-0.07±0.34
23883	26.47	33.35	2382.00	2970.00	1.25	-1.14±0.15
24281	36.08	43.74	2382.00	2970.00	1.25	-1.18±0.33
24331	120.65	138.09	2382.00	2970.00	1.25	-1.00±0.16
27211	35.54	38.59	2382.00	2970.00	1.25	-1.70±0.19
27884	26.79	36.93	2382.00	2970.00	1.25	-1.04±0.19
32644	79.98	83.67	2382.00	2970.00	1.25	-2.03±0.25
			IP-Narrow-band			
552	81.97	11.90	1396.00	998.00	0.71	-1.54±0.57
578	90.95	15.73	1416.00	1038.00	0.73	0.60±0.11
5723	380.92	59.07	1524.00	1254.00	0.82	-1.67±0.46
7082	99.60	16.25	1380.00	966.00	0.70	-0.77±0.5
11405	229.34	37.09	1499.50	1205.00	0.80	-1.18±0.45
13783	107.22	16.30	1294.00	794.00	0.61	-3.19±0.45
13863	184.08	26.83	1299.00	804.00	0.62	-2.17±0.95
16617	126.29	12.99	1228.00	662.00	0.54	-3.92±0.45
20814	169.95	26.45	1332.50	871.00	0.65	-3.09±0.45
21192	206.55	29.45	1402.00	1010.00	0.72	-1.78±0.5
23330*	197.48	33.60	1432.00	1070.00	0.75	-2.66±0.55

 doi:10.20944/preprints202604.1002.v1

24375	168.30	29.39	1530.50	1267.00	0.83	-2.85±0.55
25523	110.47	20.00	1274.00	754.00	0.59	-3.26±0.69
26138	112.47	14.14	1235.00	676.00	0.55	-2.18±0.36
26496	124.93	15.46	1366.00	938.00	0.69	-1.40±0.37
28059	138.73	25.02	1457.50	1121.00	0.77	-2.18±0.64
29808	161.04	24.48	1381.50	969.00	0.70	-1.79±0.25
30268	121.05	16.41	1403.50	1013.00	0.72	0.16±0.38
MP-broadband						
14956	126.18	26.79	2382.00	2970.00	1.25	-1.82±0.13
22556	142.62	50.68	2382.00	2970.00	1.25	-2.00±0.22

Note: * Radiation windows exist in both the main pulse and interpulse phases within one pulse period.

References

1. Pacini, F. Energy emission from a neutron star. *Nature* **1967**, *216*(5115), 567–568.
2. Goldreich, P.; Julian, W.H. Pulsar electrodynamics. *Astrophys. J.* **1969**, *157*, 869.
3. Staelin, D.H.; Reifenstein III, E.C. Pulsating radio sources near the Crab Nebula. *Science* **1968**, *162*(3861), 1481–1483.
4. Hankins, T.H.; Kern, J.S.; Weatherall, J.C.; Eilek, J.A. Nanosecond radio bursts from strong plasma turbulence in the Crab pulsar. *Nature* **2003**, *422*(6928), 141–143.
5. Rudnitskii, A.G.; Karuppusamy, R.; Popov, M.V.; Smirnova, T.V. Studies of cosmic plasma using Radioastron VLBI observations of giant pulses of the pulsar B0531+21. *Astron. Rep.* **2016**, *60*(2), 211–219.
6. Cordes, J.M.; Bhat, N.D.R.; Hankins, T.H.; McLaughlin, M.A.; Arzoumanian, Z. The brightest pulses in the Universe: multifrequency observations of the Crab pulsar's giant pulses. *Astrophys. J.* **2004**, *612*(1), 375–388.
7. Popov, M.V.; Stappers, B. Statistical properties of giant pulses from the Crab pulsar. *Astron. Astrophys.* **2007**, *470*(3), 1003–1007.
8. Mickaliger, M.B.; McLaughlin, M.A.; Lorimer, D.R.; Cordes, J.M.; Purandi, A. A giant sample of giant pulses from the Crab pulsar. *Astrophys. J.* **2012**, *760*(1), 64.
9. Hankins, T.H.; Eilek, J.A. Radio emission signatures in the Crab pulsar. *Astrophys. J.* **2007**, *670*(1), 693–701.
10. Hankins, T.H.; Eilek, J.A.; Jones, G. The Crab pulsar at centimeter wavelengths. II. Single pulses. *Astrophys. J.* **2016**, *833*(1), 47.
11. Karuppusamy, R.; Stappers, B.W.; van Straten, W. Giant pulses from the Crab pulsar—A wide-band study. *Astron. Astrophys.* **2010**, *515*, A36.
12. Thulasiram, P.; Lin, H.H. Narrow-band giant pulses from the Crab pulsar. *Mon. Not. R. Astron. Soc.* **2021**, *508*(2), 1947–1953.
13. Hobbs, G.; Manchester, R.N.; Dunning, A.; George, D.; Jameson, A.; van Straten, W. An ultra-wide bandwidth (704 to 4032 MHz) receiver for the Parkes radio telescope. *Publ. Astron. Soc. Aust.* **2020**, *37*, e012.
14. Lundgren, S.C.; Cordes, J.M.; Ulmer, M.; Armal, Z. Giant pulses from the Crab pulsar: a joint radio and gamma-ray study. *Astrophys. J.* **1995**, *453*, 433.
15. Manchester, R.N.; Hobbs, G.; Bailes, M.; Coles, W.A.; Keith, M.J.; Shannon, R.M.; Bhat, N.D.R.; Brown, A.; Burke-Spolaor, S.; Champion, D.J.; et al. The Parkes Pulsar Timing Array Project. *Publ. Astron. Soc. Aust.* **2013**, *30*, e017.
16. van Straten, W.; Bailes, M. DSPSR: digital signal processing software for pulsar astronomy. *Publ. Astron. Soc. Aust.* **2011**, *28*(1), 1–14.
17. van Straten, W.; Demorest, P. Pulsar data analysis with PSRCHIVE. arXiv preprint **2012**, arXiv:1205.6276.
18. van Straten, W.; Demorest, P.; Khoo, J.; Osłowski, S.; van Eldik, M. PSRCHIVE: development library for the analysis of pulsar astronomical data. Astrophysics Source Code Library **2011**, ascl:1105.014.
19. Fridman, P.A.; Baan, W.A. RFI mitigation methods in radio astronomy. *Astron. Astrophys.* **2001**, *378*(1), 327–344.
20. Jessner, A.; Słowikowska, A.; Klein, B.; Karuppusamy, R. Giant radio pulses from the Crab pulsar. *Adv. Space Res.* **2005**, *35*(6), 1166–1171.
21. Maron, O.; Kijak, J.; Kramer, M.; Wielebinski, R. Pulsar spectra of radio emission. *Astron. Astrophys. Suppl. Ser.* **2000**, *147*(2), 195–203.

 doi:10.20944/preprints202604.1002.v1

22. Weltevrede, P.; Johnston, S. The population of pulsars with interpulses and the implications for beam evolution. *Mon. Not. R. Astron. Soc.* **2008**, *387*(4), 1755–1760.
23. Kramer, M.; Karastergiou, A.; Gupta, Y.; Johnston, S.; Koribalski, B. Simultaneous single-pulse observations of radio pulsars—IV. Flux density spectra of individual pulses. *Astron. Astrophys.* **2003**, *407*(2), 655–668.
24. Zhang, G.Q.; Wang, P.; Wu, Q.; Li, D.; Zhang, C.; Wang, H.; Yan, Y. Energy and waiting time distributions of FRB 121102 observed by FAST. *Astrophys. J. Lett.* **2021**, *920*(1), L23.
25. Wang, H.; Wen, Z.; Wang, N.; Liu, Z. Waiting Time Distribution of Giant Pulses from the Crab Pulsar Modeled with a Non-stationary Poisson Process. *Acta Astron. Sin.* **2024**, *65*(2), 19.
26. Weibull, W. A Statistical Distribution Function of Wide Applicability. *J. Appl. Mech.* **1951**, *18*(3), 293–297.
27. Cao, G.; Yang, X.; Zhang, L. The Modeling of Pulsar Magnetosphere and Radiation. *Universe* **2024**, *10*(3), 130.
28. Petroff, E.; Bailes, M.; Barr, E.D.; Bateman, T.; Bhat, N.D.R.; Bhandari, S.; Burgay, M.; Burke-Spolaor, S.; Caleb, M.; Champion, D.J.; et al. A real-time fast radio burst: polarization detection and multiwavelength follow-up. *Mon. Not. R. Astron. Soc.* **2015**, *447*(1), 246–255.
29. Lyubarsky, Y. A model for fast extragalactic radio bursts. *Mon. Not. R. Astron. Soc. Lett.* **2014**, *442*(1), L9–L13.
30. Cerutti, B.; Philippov, A.; Parfrey, K.; Spitkovsky, A. Particle acceleration in axisymmetric pulsar current sheets. *Mon. Not. R. Astron. Soc.* **2015**, *448*(1), 606–619.
31. Lyutikov, M. On generation of Crab giant pulses. *Mon. Not. R. Astron. Soc.* **2007**, *381*(3), 1190–1196.
32. Melikidze, G.I.; Pataraia, A.D. Relativistic Langmuir soliton in the magnetosphere of pulsars. *Astrofizika* **1980**, *16*, 161–167.
33. Asseo, E.; Melikidze, G.I. Non-stationary pair plasma in a pulsar magnetosphere and the two-stream instability. *Mon. Not. R. Astron. Soc.* **1998**, *301*(1), 59–71.
34. Melikidze, G.I.; Gil, J.A.; Pataraya, A.D. The spark-associated soliton model for pulsar radio emission. *Astrophys. J.* **2000**, *544*(2), 1081–1096.
35. Geyer, M.; Serylak, M.; Abbate, F.; Buchner, S.; Chen, W.; Cumming, A.; Dai, Z.; Darwish, M.; Fender, R.P.; Gaensler, B.M.; et al. The Thousand-Pulsar-Array programme on MeerKAT–III. Giant pulse characteristics of PSR J0540-6919. *Mon. Not. R. Astron. Soc.* **2021**, *505*(3), 4468–4482.